Study of radial heat transport in W7-X using the Transfer Entropy

B.Ph. van Milligen[1], U. Hoefel[2], J.H. Nicolau[3], M. Hirsch[2], L. García[3], B.A. Carreras[3], C. Hidalgo[1] and the W7-X Team

[1] CIEMAT - Laboratorio Nacional de Fusión, Avda. Complutense 40, 28040 Madrid, Spain
[2] Max-Planck Institute for Plasma Physics, Greifswald, Germany
[3] Universidad Carlos III, 28911 Leganés, Madrid, Spain

Abstract. In this work, we analyze data obtained using the Electron Cyclotron Emission radiometer at the Wendelstein 7-X stellarator using a relatively new technique: the Transfer Entropy. Thus, we detect the propagation of information and find that it occurs in a stepwise fashion: we observe both 'trapping zones' and radial 'jumps', when the information is apparently skipping over intermediate positions. Using scans of the rotational transform, we observe that the 'trapping zones' appear to be associated with rational surfaces. Power scan experiments show that these 'jumps' increase in importance when power is increased, thus enhancing the effective diffusivity. The observations are interpreted in terms of a resistive Magneto-HydroDynamic model, which displays behavior similar to the experimental results. The 'trapping zones' are explained in terms of zonal flows associated with rational surfaces, while the 'jumps' are ascribed to mode coupling effects, i.e., the transmission of turbulent energy via the magnetic field.

PACS numbers: 52.25.Fi,52.25.Os,52.35.Ra,52.55.Hc

1. Introduction

The understanding and control of heat transport in fusion plasmas is vital to the development of efficient future fusion-based power plants, as a reduction of heat transport may evidently lead to more compact and cost-efficient reactors.

The propagation of small perturbations is a proven technique to probe transport in many physical systems. It has been known for a long time that spontaneous electron temperature fluctuations arise in Electron Cyclotron Resonance Heated (ECRH) plasmas [1], even though their origin has only partly been clarified [2]. Recent work performed in the TJ-II stellarator showed that a new analysis technique (based on the Transfer Entropy) makes it feasible to exploit these small temperature fluctuations to effectively probe heat transport [3].

In this work, we apply the same technique to Electron Cyclotron Emission (ECE) data obtained in the W7-X stellarator during its initial experimental campaign. W7-X has a larger minor radius (0.5 m vs. 0.2 m) and more ECE channels (32 vs. 12), thus offering better resolution than TJ-II for these studies. Qualitatively, the results obtained here mirror the results obtained for TJ-II to a large extent, suggesting that heat transport may be governed by the same principles in a small (non-optimized) device such as TJ-II and a large (optimized) device such as W7-X, even though global transport levels are very different. Both devices are low-shear stellarators, offering a low density of low-order rational surfaces which facilitates the study of the impact of such surfaces on transport. With its significantly larger minor radius and its enhanced ECE diagnostic, W7-X offers an ideal platform for these studies.

We make use of a resistive Magneto-HydroDynamic model to aid the interpretation and provide support for some of the experimental observations on W7-X reported here.

We find that heat transport is not a continuous process but occurs stepwise. In the vicinity of major rational surfaces, 'trapping zones' tend to form where radial transport is slowed down (mini-transport barriers associated with zonal flows [4, 5]). On the other hand, transport is also observed to occur rapidly, sometimes apparently 'jumping over' intermediate positions. Based on modelling results, we associate the 'trapping zones' with local flow shear maxima, while we ascribe the rapid radial transport (reminiscent of avalanches [6]) to mode coupling effects.

This paper is organized as follows. Section 2 describes the experimental setup and analysis techniques used. Section 3 reports the experimental results. Section 4 presents a model used to facilitate the interpretation of the experimental results. Finally, Section 5 puts the results into context and discusses their significance and implications.
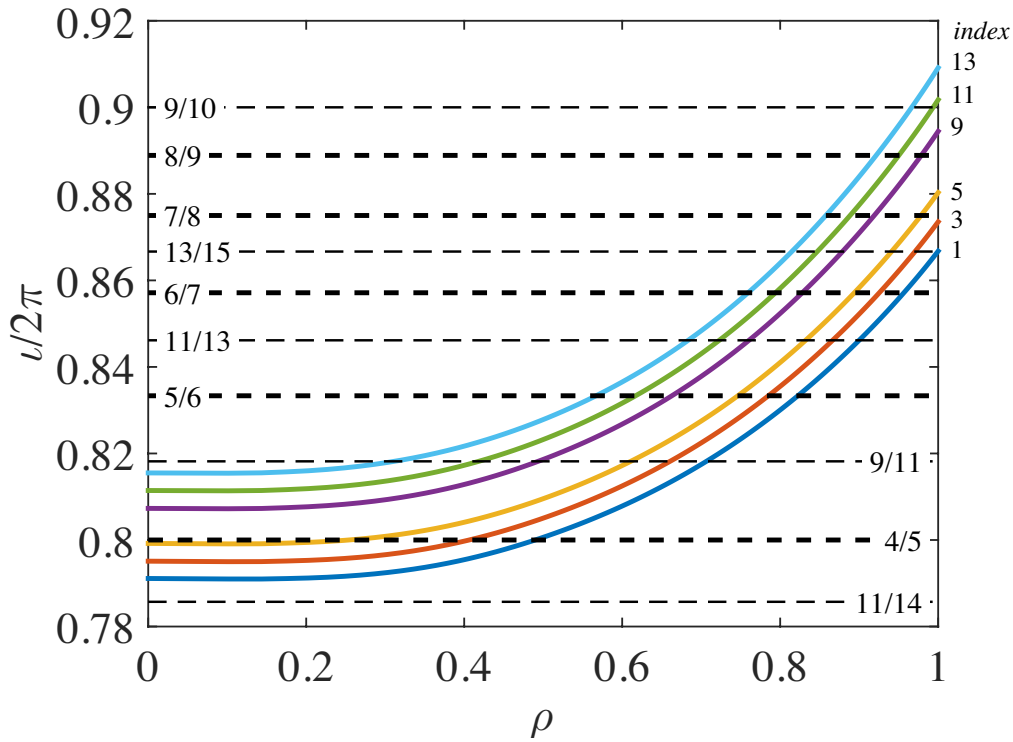
Figure 1. Profiles of the rotational transform, $\iota = \iota/2\pi$, as a function of normalized radius, $\rho = r/a$, for the set of magnetic configurations studied here. The lowest ι profile (index 1) corresponds to the 'standard OP1.1' configuration. Major rational values are indicated by horizontal dashed lines.

2. Experimental setup and analysis techniques

Wendelstein 7-X is a helical advanced stellarator (HELIAS) with major radius $R = 5.5$ m, minor radius $a \simeq 0.5$ m, 5 field periods, and a toroidal magnetic field of up to $\simeq 3$ T. The design of the device was based, among others, on the optimization of Neoclassical particle transport and MHD stability [7, 8].

This work focuses on a set of discharges from the first operational phase of W7-X [9]. These discharges are characterized by low electron density ($\overline{n_e} \simeq (1-2) \cdot 10^{19}$ m^{-3}) and are heated by Electron Cyclotron Resonance Heating (ECRH, $P_{\mathrm{ECRH}} = (0.6 - 2)$ MW), resulting in so-called Core Electron Root Confinement (CERC) plasmas [10].

2.1. Magnetic configurations

Among others, we will analyze data from a set of discharges corresponding to a $\iota = \iota/2\pi$ scan. The relevant ι profiles are shown in Fig. 1. The vacuum magnetic configurations are identified by an index number, such that the six iota profiles shown correspond to index values (bottom to top): 1, 3, 5, 9, 11, 13.
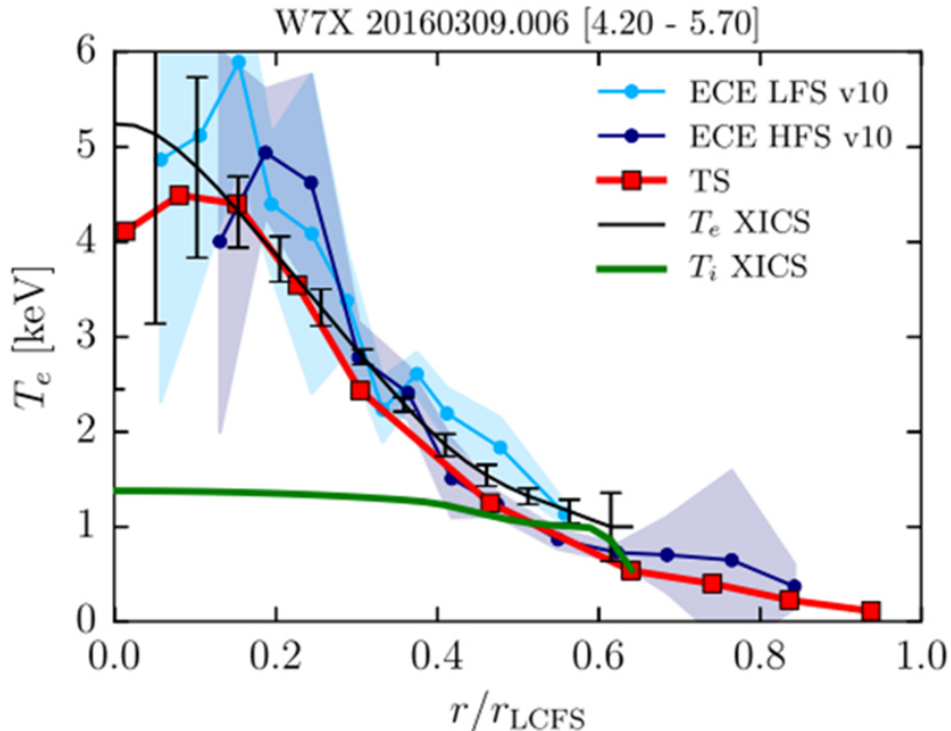
Figure 2. Typical profiles for the discharges used here, at low ECR heating power (0.6 MW). Figure reproduced from [13] with permission.

These discharges have relatively low pressure and a small amount of bootstrap current [11], which imply a shift of the flux surfaces and a slight modification of the iota profile. According to neoclassical estimates [12], in the radial range of interest here ($0.4 < \rho < 0.8$), the shift induced by the bootstrap current is limited to $|\Delta\rho| < 0.06$, while $\Delta\rho = 0$ at $\rho \simeq 0.6$. As the features we will be discussing below have a similar radial extent, the indicated vacuum locations of rational surfaces, without bootstrap contribution, may be considered sufficiently accurate within the available resolution. A correction for the shift of the flux surfaces is discussed below.

2.2. Heating

Plasmas are heated using Electron Cyclotron Resonance Heating with up to about 4 MW total power, deposited on axis [13]. Typical profiles with central power deposition are shown in Fig. 2.

2.3. Electron Cyclotron Emission diagnostic

We mainly use data from the W7-X ECE diagnostic [14, 15]. It disposes of 32 channels, covering large part of the minor plasma radius. Analysis results will be shown as a

function of the normalized radius $\rho = r/a$, such that negative values of ρ correspond to the low field side of the plasma, and positive values to the high field side.

We will analyze the radial propagation of spontaneous temperature fluctuations arising in the core plasma, as well as heat waves produced by ECRH modulation.

2.4. Temperature perturbations

In ECR heated discharges, spontaneous temperature perturbations appear [1] (see Section 3.2). Regarding the origin of these fluctuations, we note the following. (a) The ECRH power source itself may fluctuate in time. (b) Spontaneous density fluctuations in the plasma (associated with turbulence or filaments [16]) may lead to fluctuations in power absorption and hence temperature perturbations. In Section 3.1, it is shown that temperature perturbations are correlated along a flux surface, implying very long correlation lengths along field lines [17], reinforcing the filamentary hypothesis and consistent with Ref. [2]. It has been speculated that the density fluctuations may be due to resistive interchange modes, possibly driven by fast electrons [18].

2.5. The Transfer Entropy

To analyze the propagation of temperature fluctuations, traditional heat pulse analysis techniques (correlation, conditional averaging [19]) do not offer sufficient clarity: the correlation tends to smear out the information over the typical duration of the heat pulses, while the conditional averaging technique tends to offer poor statistics due to the necessity to clearly identify individual (relatively large) events.

For this reason, we turn to a technique from the field of Information Theory [20] that was recently applied for the first time in the context of fusion plasmas [21]: the Transfer Entropy. This nonlinear technique measures the 'information transfer' between two signals, is directional, and uses all the information available in the two signals, regardless of amplitude or sign.

The Transfer Entropy is a measure of the causal relation or information flow between two time series. In this work, we use a simplified version of the Transfer Entropy:

$$T_{Y \to X} = \sum p(x_{n+1}, x_{n-k}, y_{n-k}) \log_2 \frac{p(x_{n+1}|x_{n-k}, y_{n-k})}{p(x_{n+1}|x_{n-k})}. \tag{1}$$

Here, $p(a|b)$ is the probability distribution of a conditional on b, $p(a|b) = p(a,b)/p(b)$. The probability distributions $p(a, b, c, \ldots)$ are constructed using m bins for each argument, i.e., the object $p(a, b, c, \ldots)$ has m^d bins, where d is the dimension (number of arguments) of p. The sum in Eq. 1 runs over the corresponding discrete bins. The number k can be converted to a 'time lag' by multiplying it by the sampling rate. The construction of the probability distributions is done using 'coarse graining', i.e., a low number of bins (here, $m = 3$), to obtain statistically significant results. For more information on the technique, please refer to Ref. [21]. The value of the Transfer Entropy T, expressed in bits, can be compared with the total bit range, $\log_2 m$, equal

to the maximum possible value of T, to help decide whether the Transfer Entropy is significant or not.

The statistical significance of the Transfer Entropy can be estimated by calculating T for two random (noise) signals [22]. Here, we will be analyzing signals with a typical duration between 0.2 and 0.3 s (or up to nearly 2 s for modulated discharges) at a sampling rate of up to 2 MHz, corresponding to $4 \cdot 10^5 \leq N \leq 6 \cdot 10^5$ samples, so that the statistical significance level of T is well below 10^{-4}.

The Transfer Entropy measures the *increase of degree of predictability* of the next temporal sample of signal x, given historical information from both signals x and y, as compared to the degree of predictability given only historical information from signal y itself. In this paper, 'historical information' is simply the value of the sample at time $t - \Delta t$, where $\Delta t = k/f_{\mathrm{samp}}$ is the 'time lag' (f_{samp} being the sampling frequency). The complete set of historical information would correspond to the whole available range of Δt values, from 0 up to a maximum value determined by the available samples of the data array. Therefore, the Transfer Entropy calculated using only one historical sample corresponds to only a fraction of the available predictive capacity that can be obtained from all historical information; hence it is not unreasonable that the obtained values of the Transfer Entropy are generally not close to the maximum value possible, $\log_2 m$. On the other hand, using a single lag value offers the advantage that it is easy to deduce an 'information propagation speed' that can be fruitfully compared to the expected propagation speeds for heat transport.

The Transfer Entropy has some remarkable properties. First, it is directional, a fact that provides an additional filter that preferentially selects information components related to (directional) propagation. Second, unlike linear tools such as the cross correlation or the conditional average, it does not depend on the temporal waveform or even the amplitude of the fluctuations, but merely on the time lag between x and y. This converts the technique in an exquisitely sensitive tool to study the propagation of perturbations in highly non-linear systems (such as fusion plasmas), in which perturbations tend to be deformed or change shape quickly as they propagate.

However, we emphasize that the 'propagation of information' is not the same as the 'propagation of heat pulses', as the former does not depend on signal amplitude, while the latter does. On the other hand, diffusion is a geometrical quantity: it measures the spread (distance squared) in time of an initially concentrated perturbation. Thus, even though the Transfer Entropy is a measure of 'information transport' and not 'heat transport', it should still be possible to extract the geometrical properties of this spreading and hence a diffusion coefficient. As the underlying measurements are electron temperature fluctuations, one may expect this geometrical spreading to be relevant to the topic of 'heat transport'.
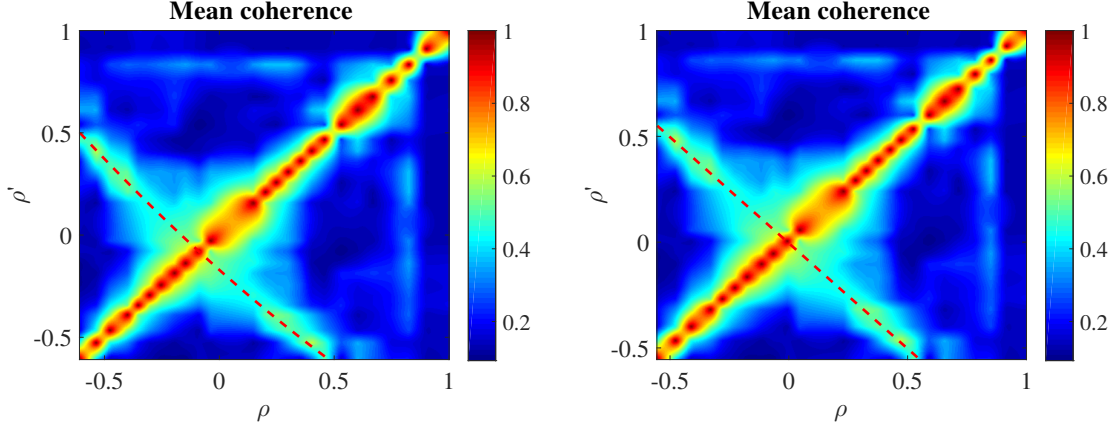
Figure 3. a) Left: Mean coherence between all ECE channels versus the nominal ρ values of the channels. b) Right: The same, but after applying the ρ correction discussed in the text. Note that the dotted appearance of the auto-coherence (along the line $\rho' = \rho$) is an artifact of the interpolation method used.

3. Experimental results

3.1. Identification of flux surface shift

The location of the rational surfaces may deviate from the calculated ('nominal') location, obtained in a reference discharge, due to finite β effects or (bootstrap) currents in the plasma. To identify the rational surfaces, we apply a simple technique, consisting of calculating the coherence between ECE channels.

Fig. 3 shows the mean coherence $\overline{\gamma_{xy}}$ between any two ECE channels (x and y, located at 'nominal positions' ρ and ρ', respectively), defined as:

$$\overline{\gamma_{xy}} = \frac{\int S_{xy}^2(\omega)\gamma_{xy}(\omega)d\omega}{\int S_{xy}^2(\omega)d\omega} \tag{2}$$

where $S_{xy}^2(\omega)$ is the spectral cross power, $S_{xy}^2 = \sqrt{|S_x^2||S_y^2|}$, and the spectral coherence is

$$\gamma_{xy}(\omega) = \frac{|\langle S_x(\omega)S_y^*(\omega)\rangle|}{\sqrt{\langle S_x^2(\omega)\rangle\langle S_y^2(\omega)\rangle}} \tag{3}$$

where rectangular brackets refer to an ensemble average over successive time intervals.

Fig. 3a shows two main features: 1) a strong diagonal feature (at $\rho' = \rho$), corresponding to the auto-coherence, which is 1 by definition; and 2) a linear feature at near right angles, close to the line $\rho' = -\rho$, corresponding to the coherence between channels on the same flux surface, but on opposite sides of the magnetic axis. Due to the fact that the 'nominal ρ' values correspond to a discharge (160302.008, 3.2–3.7 s) with slightly different pressure (β) than the one studied in this case (160309.011, 0.08–0.38 s), a slight deviation from the line $\rho' = -\rho$ occurs, similar to a 'Shafranov shift'.

The perpendicular linear feature seen in Fig. 3a can be modeled as $\rho' = -\rho + b(1 - \rho^2)$, shown in this figure as a dashed line. This fit can be used to correct the 'nominal ρ' values to account for the Shafranov shift, by defining

$\rho_{\text{new}} = \rho_{\text{old}} + \Delta(1 - \rho_{\text{old}}^2)$, where $\Delta = -b/2$. The result of this correction is shown in Fig. 3b. The correction implicitly assumes that the B-field is not modified significantly with respect to the reference equilibrium (on which the 'nominal' ECE radii are based), even in the presence of the additional Shafranov shift of the flux surfaces.

The figures in the remainder of the paper show ρ values that are corrected for the Shafranov shift using this coherence technique.

3.2. Radial propagation of core perturbations

To visualize radial propagation (of information), we have calculated the Transfer Entropy in a number of discharges with different conditions, between a reference ECE channel and all other available ECE channels. Within each discharge, the ECRH heating power was varied. An initial 'high power' phase (ECRH power $P_{\text{ECRH}} \simeq 2.0$ MW) was followed by a 'low power' phase ($P_{\text{ECRH}} \simeq 0.6$ MW) and a 'medium power' phase ($P_{\text{ECRH}} \simeq 1.3$ MW), each phase lasting about 0.3 s. The discharges correspond to different magnetic configurations and ι profiles (cf. Fig. 1), such that rational surfaces are placed at different radial locations (as indicated in the figures below). The vertical axes and rational surfaces shown in the figures of this section always correspond to the nominal ρ values of the ECE channels, corrected for the Shafranov shift according to the method of Section 3.1. Line average density was relatively low in these discharges ($\overline{n}_e \simeq 1.5 \cdot 10^{19}$ m^{-3}).

We are most interested in outward propagation. Therefore, we use a reference channel located close to $\rho = 0.2$, not far outside the central ECRH power deposition region.

To clarify and emphasize the advantages of our approach, we first compare results from the Transfer Entropy and the standard cross correlation. This comparison is shown in Fig. 4. While the Transfer Entropy is a fully non-linear analysis, the correlation analysis is linear and therefore perhaps not ideally suited for the analysis of turbulence. This is reflected in the low values of the correlation, which would normally not be considered significant, except for the relatively high values occurring at time lag $\tau = 0$ (around 0.5, exceeding the maximum value of the color scale shown; recall that these correlation values were used in Section 3.1 for the correction of ρ values). However, we note that the general pattern of the correlation for time lags $\tau > 0$ and radii $\rho > 0.2$ bears a striking similarity to the Transfer Entropy results, which gives confidence that the Transfer Entropy results are physically meaningful. The large value of the Transfer Entropy with respect to the statistical significance level (around 10^{-4}, see Section 2.5) should be noted. This example shows to what degree the nonlinear Transfer Entropy supersedes the linear correlation when analyzing the propagation of small, irregular heat pulses.

Fig. 5 shows the result of the analysis for two discharges with the same configuration, which can be used to provide an indication of the reproducibility of results. Although reproducibility is not perfect, clearly some of the main features are similar
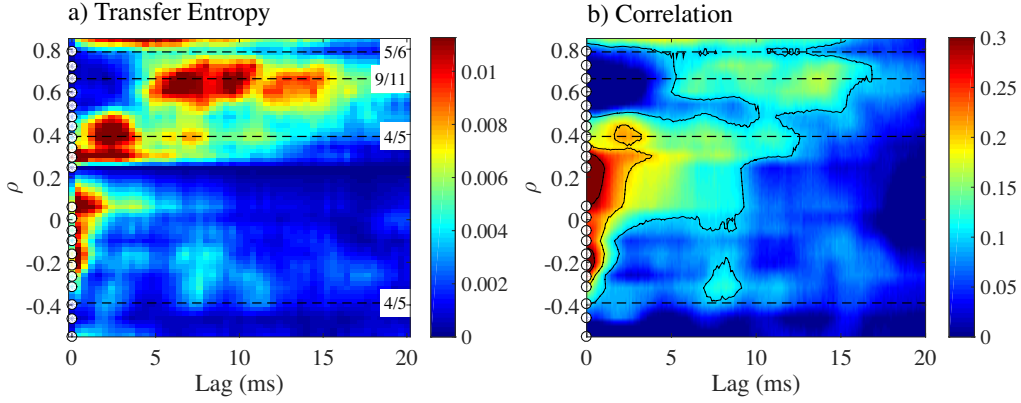
Figure 4. Transfer Entropy and cross correlation vs. ρ and time lag, τ, for discharge 20160309.016. Configuration index: 3 (cf. Fig. 1). In this and the following figures, dots on the left-hand axis indicate the location of ECE measurement channels, while horizontal dashed lines indicate the location of rational surfaces. Some contour lines have been added for clarity.

among these discharges and heating levels, in particular the indicated 'plume' (thick dashed line) moving outward from $|\rho| \simeq 0.2$ to the 4/5 rational surface, very similar in shape, width, and propagation speed between the two discharges. High values of TE at $\rho \simeq 0.85$ in the high power case should be ignored, as these can be ascribed to the low frequency tail of 3$^{\text{rd}}$ harmonic emission with small optical depth, so that these measurements do not correspond to local temperatures. On the other hand, the low/high field side asymmetry in the high power phase could be caused by relatively strong emission from hot core electrons, contaminating the low field side data. In the following, we will therefore focus on the remaining data ($0 < \rho < 0.85$). We emphasize that the Transfer Entropy in this radial range tends to peak at time lag values that are consistent with typical time delays expected from the background heat transport coefficient, which gives confidence that these results are relevant for the heat transport studies at hand.

Generally speaking, the Transfer Entropy reaches higher values in the high power phase, which is attributed to a larger number of perturbations originating propagation. It is noteworthy that the 4/5 rational surface seems to constitute an 'attractor' (or 'trapping zone') for this outward plume. In addition, a strong response is seen near the 9/11 rational surface (at time lags between 3 and 12 ms) in the high power cases. This suggests that the core perturbations, which may be assumed to be of larger amplitude in the high power cases, trigger a response near this 9/11 surface, located further outward.

Fig. 6 shows the results from a discharge with a different magnetic configuration (note that the rational surfaces have moved slightly with respect to the preceding
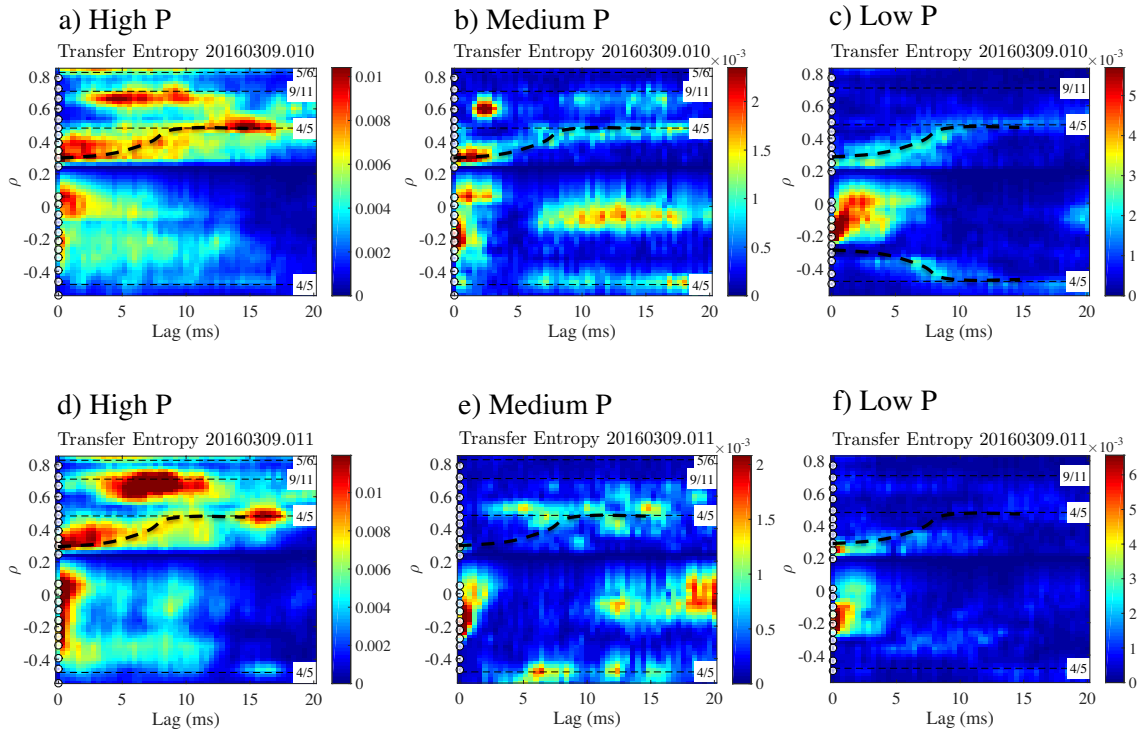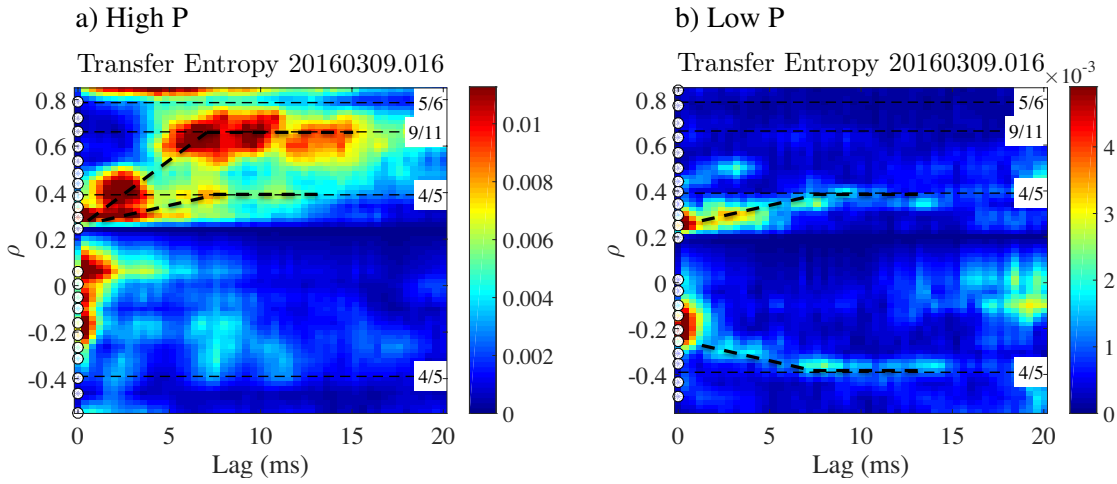
Figure 5. Transfer Entropy vs. ρ and time lag, τ, for equivalent discharges 20160309.010 (a-c) and 20160309.011 (d-f), at three different power levels (see text). Configuration index: 1 (cf. Fig. 1). Radial propagation is indicated with thick dashed lines.

figure). Comparing the low and high ECRH power phases, one observes that they have in common that some perturbations propagate outward relatively slowly to the 4/5 rational surface, which acts as a 'trapping zone' for these perturbations, similar to Fig. 5. In the high power phase, there is an additional branch of radial propagation, faster and more intense (in terms of information transfer), reaching the 9/11 rational surface.

Fig. 7 shows a similar result, again in a different magnetic configuration, for three ECRH power levels. Propagation is outward from $|\rho| \simeq 0.2$ until the position of the 9/11 rational surface is reached. The latter position acts as a 'trapping zone' for the outward propagation of information.

Summarizing the observations so far, the outward propagation of the temperature perturbations (more precisely: the causal impact of central temperature fluctuations on fluctuations further outward) is detected with clarity and shows up as a more or less 'diagonal plume' corresponding to outward propagation starting at the reference position, $|\rho| \simeq 0.2$. The typical radial propagation speed is approximately 0.5 m (the minor radius) in 20 ms, or 25 m/s. This can be compared to the result for TJ-II, where speeds in the order of 100–200 m/s were obtained [3].
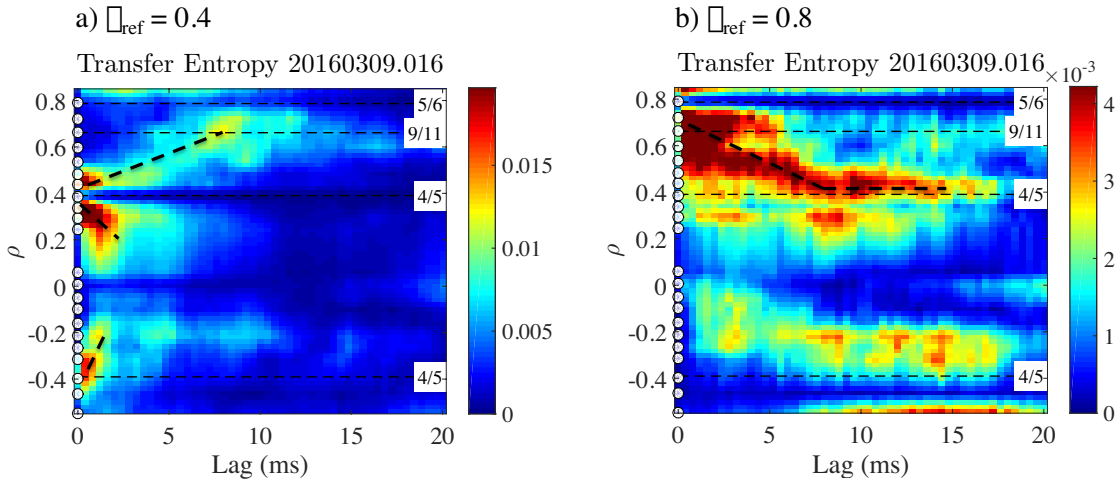
Figure 6. Transfer Entropy vs. ρ and time lag, τ, for discharge 20160309.016. Configuration index: 3 (cf. Fig. 1). Radial propagation is indicated with thick dashed lines.
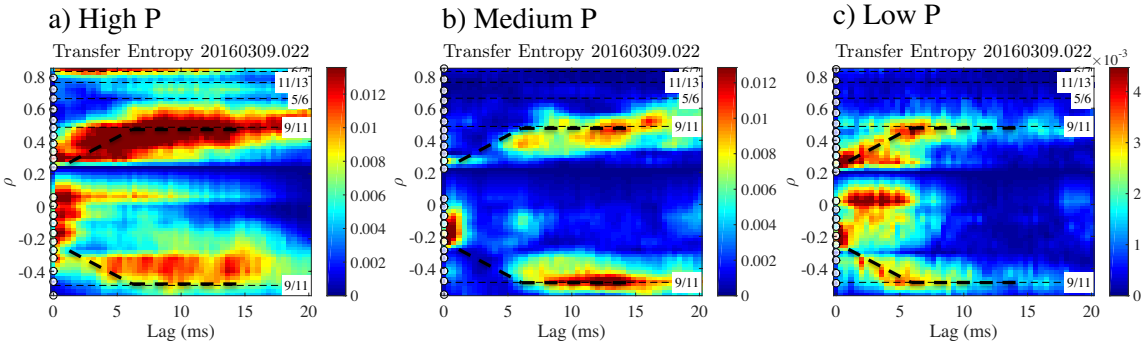
Figure 7. Transfer Entropy vs. ρ and time lag, τ, for discharge 20160309.022. Configuration index: 9 (cf. Fig. 1). Radial propagation is indicated with thick dashed lines.

The figures show that propagation is not continuous, but experiences delays ('trapping') at certain radial positions, which appear to be associated with low-order rational surfaces, within the available resolution. Also, apparent propagation 'jumps' occur, when the response at a given outward location is more intense than at some other locations further inward. This is exemplified by Fig. 6, in which two transport branches may be discerned: (a) relatively slow outward propagation up to the 4/5 rational surface, visible in both the low and high ECRH power phases, and (b) much faster radial propagation, apparently discontinuous, reaching the 9/11 rational surface, only apparent in the high power phase. This result seems to suggest that an additional transport channel is activated at increased heating power; therefore, this effect might be related to the phenomenon of power degradation.

Some figures seem to suggest that different rational surfaces may be affecting transport simultaneously. E.g., in Figs. 5 and 6, the left graphs (high power) seem to show that both the 4/5 and 9/11 rational surfaces are associated with transport barriers or 'trapping zones'.

Figure 8. Transfer Entropy vs. ρ and time lag, τ for discharge 20160309.016 (high power phase). a) Left: reference $\rho \simeq 0.4$; b) Right: reference $\rho \simeq 0.8$. Dots indicate the location of ECE measurement channels. Horizontal dashed lines indicate the location of rational surfaces.

3.3. Radial propagation of mid-radius perturbations

In this section, we study the effect of choosing a different reference ECE channel. Fig. 8 shows two examples with reference positions taken at $\rho \simeq 0.4$ and 0.8. Starting from $|\rho| \simeq 0.4$, both inward and outward propagation is visible (indicated by the thick dashed lines). From the reference position $\rho \simeq 0.8$, inward propagation is visible. Note that the Transfer Entropy values are much lower in the latter case, suggesting that inward propagating events are more scarce.

3.4. Comparison between Transfer Entropy and the Fourier analysis of heat pulse propagation

In this section, we will study discharges with modulated ECRH. The main purpose of this exercise is to compare the Transfer Entropy results with the results from a traditional heat wave analysis using Fourier techniques [23], in order to understand the relevance of the Transfer Entropy for heat transport analysis better.

In the discharges studied here, power is modulated at $f_{\mathrm{mod}} = 17$ Hz with a modulation depth of about 35%. Fig. 9 shows the Transfer Entropy, calculated over the time window $0.35 < t < 2.0$ s, with modulated on-axis heating, along with the Fourier time delay and amplitude (cross power) using a traditional analysis based on the fundamental modulation frequency. The reference position is taken at $\rho \simeq 0$. The Fourier time delay is related to the relative phase with respect to the reference channel by $\Delta t = \Delta \phi / 2\pi f_{\mathrm{mod}}$. Outward propagation of the heat waves from the core is very clear on both sides of the magnetic axis.

Likewise, Fig. 10 shows the Transfer Entropy, calculated over the time window $0.30 < t < 1.1$ s, with modulated off-axis heating, along with the Fourier time delay and amplitude. The reference position is taken at $\rho_{\mathrm{ref}} \simeq 0.4$. The results show heat waves propagating both inward and outward from the reference position ($\rho \simeq 0.4$) and the opposite point at $\rho \simeq -0.4$.

We draw attention to the fact that the Fourier time delay values show similar radial behavior as the local Transfer Entropy maxima. In our opinion, this certifies that the Transfer Entropy time delays are the result of radial heat transport of the modulated heat wave. The precision of the Fourier results (indicated by horizontal error bars) is better than the Transfer Entropy. This is due to the fact that the Fourier results are based on a single frequency component of the modulated $T_e(\rho, t)$ signals, namely the fundamental frequency, whereas the Transfer Entropy is calculated from the unfiltered signals, and includes other frequency components as well as noise.

Of course, we have no intention to present the Transfer Entropy as an alternative to the powerful Fourier technique, but rather, we are trying to show the relevance of the Transfer Entropy to heat pulse propagation analysis. In this respect, we would like to point out that heat wave analysis based on ECRH power modulation typically involves modulation amplitudes that are sufficiently large to facilitate easy detection, which may be considered a significant perturbation of the background plasma state. On the other hand, the Transfer Entropy facilitates the analysis of the propagation of small, random perturbations, as reported in the preceding sections, and so offers a non-perturbative approach to heat pulse analysis, arguably a strong point of this technique.

Thus, we conclude that the Transfer Entropy provides essentially the same information as the phase delay obtained from modulation experiments, which justifies our interpretation of the obtained time delays (or relative phases) in terms of heat transport [24].
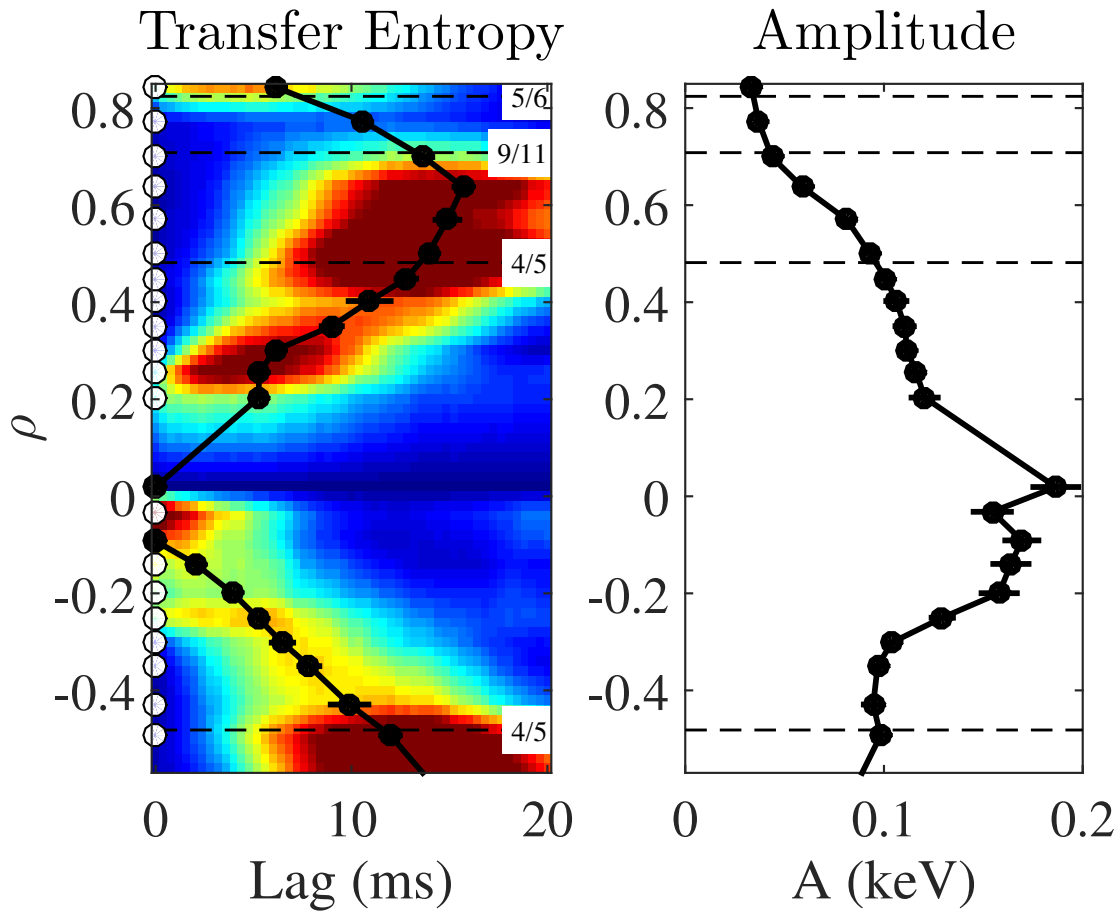
Figure 9. Comparison of Transfer Entropy (left) and Fourier analysis (time delay shown in the left panel and amplitude in the right panel as black lines with error bars) in a modulated discharge (20160302.008) with on-axis heating.
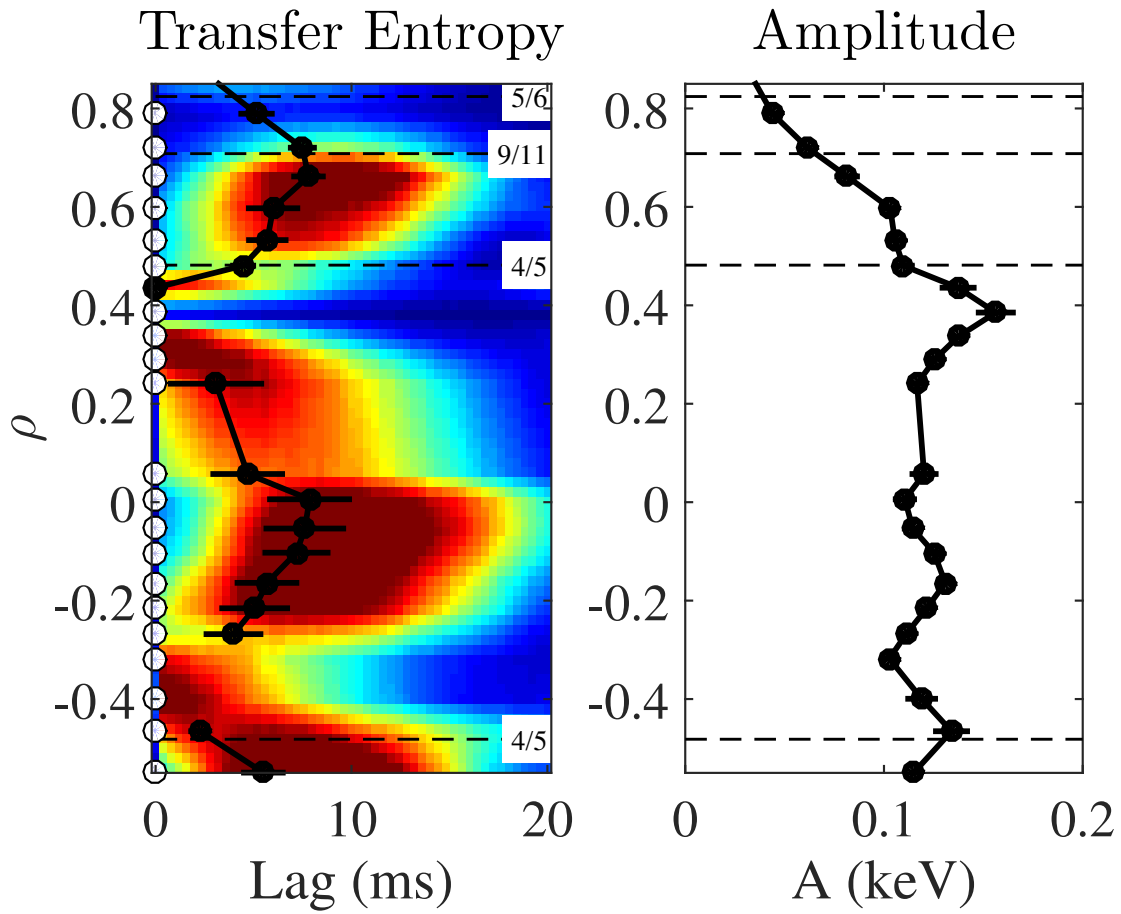
Figure 10. Comparison of Transfer Entropy (left) and Fourier analysis (time delay shown in the left panel and amplitude in the right panel as black lines with error bars) in a modulated discharge (20160308.016) with off-axis heating.

4. Modelling

In this section, we will use numerical simulations to aid the interpretation of the experimental observations presented in the previous sections. The results reported in Section 3 suggest that the observations might involve fluctuations associated with the magnetic geometry, such as resistive MHD modes. Therefore, we turn to a resistive MHD model, while emphasizing that only few plasma turbulence models include the effects of perturbations of the magnetic geometry [25], as most turbulence (and gyrokinetic) models operate in a fixed magnetic geometry for simplicity. This model is then used to study the temporal evolution of heat perturbations and the effect of self-consistent zonal flows on radial propagation. Due to the demanding nature of these simulations, the simulations are performed in a simplified mean geometry (cylindrical), and the Neoclassicial radial electric field E_r is not included. Consequently, the simulations are not intended to model W7-X in detail, but merely to provide initial and qualitative understanding of the effects on heat transport produced by the mentioned instabilities. The obvious enhancements of the simulation approach, namely including the full magnetic geometry and matching the experimental profiles more closely, are left to future work.

In devices with small magnetic shear, low-order rational surfaces have an impact over a relatively wide radial region. Their presence may facilitate the generation of magnetic islands and associated turbulent vortices, which can lead to the formation of zonal flows, which in turn affect the turbulence itself [4, 5]. The radial variation of the amplitude of such zonal flows leads to the formation of what has been called mini-transport barriers [26, 27, 28, 29, 30]. Below, we analyze the temporal evolution of a heat pulse in this complex environment. In earlier work, we performed this study for the TJ-II device, showing how these zonal flows affect the propagation of heat [3]. Now, we repeat this analysis using parameters relevant to the W7-X stellarator, which has low magnetic shear, like TJ-II, facilitating the study of the impact of low rational surfaces and zonal flows on heat propagation.

4.1. The model

We use a two-fluid resistive MHD model that has been used several times in the past to interpret results from TJ-II experiments [31, 3]. It is based on the Reduced MHD equations [32]. The dominant instabilities are pressure gradient driven modes – in particular, interchange modes. The geometry of the system is a periodic cylinder (r, θ, z) while the magnetic field line curvature κ includes the averaged effect of the toroidal and helical components of the magnetic field, where the magnetic field line curvature is given by

$$\kappa \equiv \frac{r}{R_0} B_0^2 V''. \tag{4}$$

Here, r is the radial coordinate, R_0 is an effective major radius, a is the radius of the cylinder and B_0 is the toroidal magnetic field. The prime denotes the derivative with

respect to toroidal flux, and $V' = \int dl/B$ is the specific volume enclosed by a flux surface. The model is described by the equations

$$\frac{\partial \tilde{\psi}}{\partial t} = \nabla_\parallel \phi - S\bar{\omega}_{*e} \left(\frac{T_{eq}}{n_{eq}} \nabla_\parallel n + \nabla_\parallel T_e \right) + \eta \tilde{J}_z,$$

$$\frac{\partial \tilde{U}}{\partial t} = -V_\perp \cdot \nabla U + S^2 \nabla_\parallel J_z - S^2 \frac{\beta_0}{2\varepsilon^2} \kappa \left(\frac{T_{eq}}{n_{eq}} \frac{1}{r} \frac{\partial \tilde{n}}{\partial \theta} + \frac{1}{r} \frac{\partial \tilde{T}_e}{\partial \theta} \right) + \mu \nabla_\perp^2 \tilde{U},$$

$$\frac{\partial \tilde{n}}{\partial t} = -V_\perp \cdot \nabla n + \frac{S}{\bar{\omega}_{ci}} \nabla_\parallel J_z + D_\perp \nabla_\perp^2 \tilde{n},$$

$$\frac{\partial \tilde{T}_e}{\partial t} = -V_\perp \cdot \nabla T_e + \frac{S}{\bar{\omega}_{ci}} \frac{T_{eq}}{n_{eq}} \nabla_\parallel J_z + \chi_\perp \nabla_\perp^2 \tilde{T}_e + \nabla_\parallel \left(\chi_\parallel \nabla_\parallel Te \right). \tag{5}$$

Here, ψ is the poloidal magnetic flux, U is the toroidal component of the vorticity, n is the density and T_e is the electron temperature. The tildes indicate fluctuations and the subindeces "eq" indicates the equilibrium profiles. $V_\perp$ is the perpendicular component of the velocity. $J_z = \nabla_\perp^2 \psi$ is the toroidal current and η is the resistivity. $\tilde{U} = \nabla_\perp^2 \phi/B_0$ where ϕ is the electrostatic potential. The viscosity coefficient is μ, $D_\perp$ is the perpendicular density diffusion and $\chi_\parallel (\chi_\perp)$ is the parallel (perpendicular) heat conductivity. β_0 is the ratio of the plasma pressure p and the magnetic pressure, $B_z^2/2\mu_0$, where μ_0 is the vacuum permeability. The aspect ratio is $\varepsilon = a/R_0$. The resistive time is $\tau_R = \mu_0 a^2/\eta(0)$ where $\eta(0)$ is the resistivity at the magnetic axis. The Alfvén time is $\tau_A = R_0\sqrt{\mu_0 m_i n_i}/B_z$ where m_i and n_i are the ion mass and density, respectively. The Lundquist number is $S = \tau_R/\tau_A$. The normalized frequencies appearing in the equations are $\bar{\omega}_{*e} = \tau_A \omega_{*e}$, where $\omega_{*e} = T_e/(ea^2 B_z)$ is the electron diamagnetic frequency; and $\bar{\omega}_{ci} = \tau_A \omega_{ci}$, where $\omega_{ci} = eB_z/m_i$ is the ion cyclotron frequency.

In the simulations, $S = 1.9 \times 10^6$, $\beta_0 = 6 \times 10^{-3}$, $\bar{\omega}_{*e} = 2 \times 10^{-4}$, $\bar{\omega}_{ci} = 500$ and $\varepsilon = 0.1$. The density and temperature values are normalized to the maximum density and temperature at equilibrium, respectively. Lengths are normalized to the minor radius a and times to τ_R. Please refer to Ref. [31] for more information about the model.

The evolution of the averaged electron temperature is described by

$$n_{eq} \frac{\partial \langle T_e \rangle}{\partial t} = -\frac{1}{r} \frac{\partial}{\partial r} (r\Gamma_Q) + n_{eq} \frac{1}{r} \frac{\partial}{\partial r} \left(r\chi_{0\perp} \frac{\partial \langle T_e \rangle}{\partial r} \right) + S_Q, \tag{6}$$

where the heat flux Γ_Q is

$$\Gamma_Q = n_{eq} \left\langle \tilde{V}_r \tilde{T}_e \right\rangle - \frac{S}{\bar{\omega}_{ci}} T_{eq} \left\langle \tilde{B}_r \tilde{J}_z \right\rangle - n_{eq} \left\langle \tilde{B}_r \chi_\parallel \nabla_\parallel T_e \right\rangle. \tag{7}$$

The angular brackets indicate a poloidal and toroidal angle average. V_r and B_r are the radial velocity and magnetic field, respectively. The source S_Q serves to keep the integrated electron temperature constant.

In this work, we use the "standard" magnetic configuration (index 1 in Fig. 1) such that the 4/5 rational surface is well inside the plasma and the 5/6 rational is relatively close to the edge.
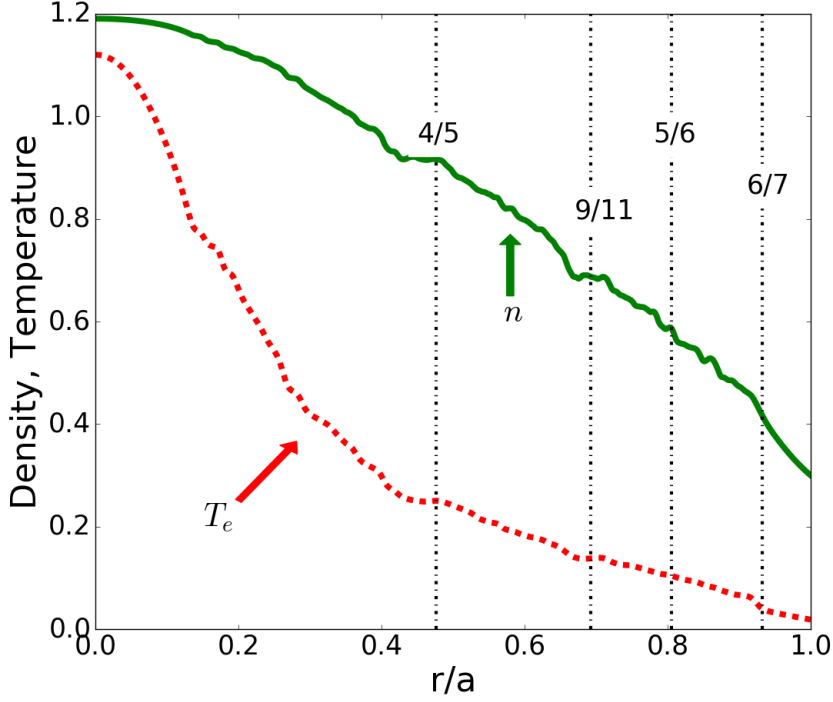
Figure 11. Steady state profiles for density and electron temperature in the standard magnetic configuration at some arbitrary time. Dashed lines indicate the position of some low order rational surfaces.

4.2. Temperature perturbations

We advance our set of equations until steady state is obtained. The profiles are kept steady with the aid of small, unchanging source terms. The steady state profiles for density and electron temperature are shown in Fig. 11.

A single instantaneous heat pulse is introduced in the plasma. Then we follow the relaxation of that perturbation over time. We run three different simulations with three different pulses. The three pulses are located at different radial locations but have the same initial shape, namely a Gaussian with peak value $T_e = 1.5$ and a narrow width of $\sigma = 0.07$. The three locations are chosen to be inside, near, and outside a suspected transport barrier. The time evolution of the three pulses is shown in Fig. 12. The left panel shows the average (angular and temporal) poloidal velocity $\langle V_\theta \rangle$. It should be noted that even in steady state, the poloidal velocity is not constant and evolves in time. However, for the duration of the heat pulses the $\langle V_\theta \rangle$ is mostly constant. The temporal average of $\langle V_\theta \rangle$ has been calculated over a time that exceeds the duration of a heat pulse by a factor of 100. The three right panels show the propagation of the pulses launched at initial locations $r/a = 0.25$, $r/a = 0.35$ and $r/a = 0.45$, respectively. The colors indicate the temperature difference between $T_e(r, t)$ and the initial $T_e^0(r)$ profile (taken immediately before the pulse).

We suggest a transport barrier is formed in the region between $r/a \approx 0.26$ and
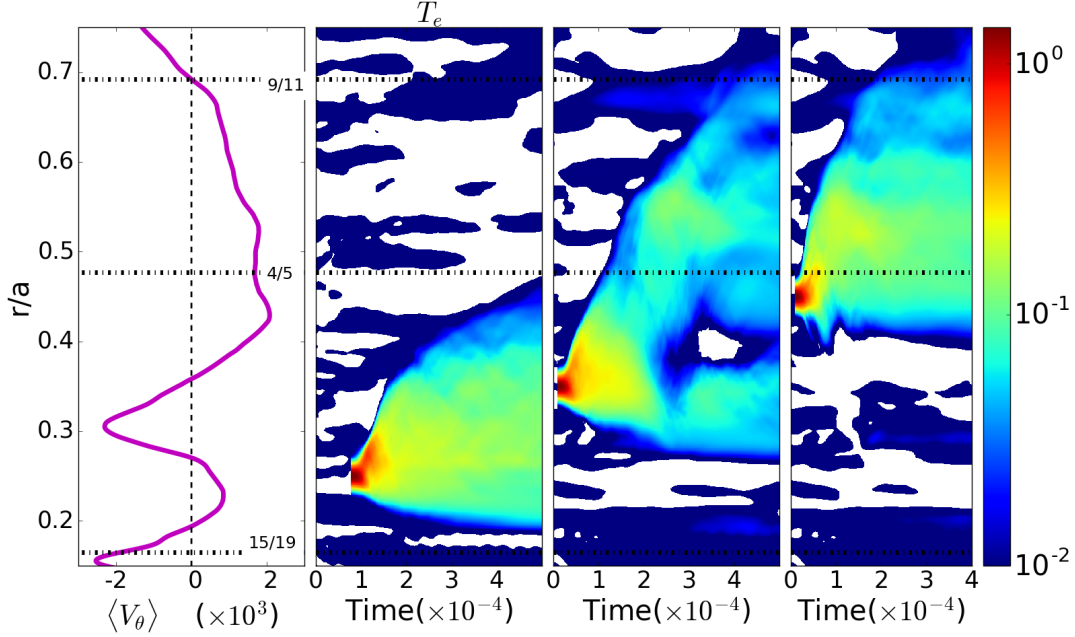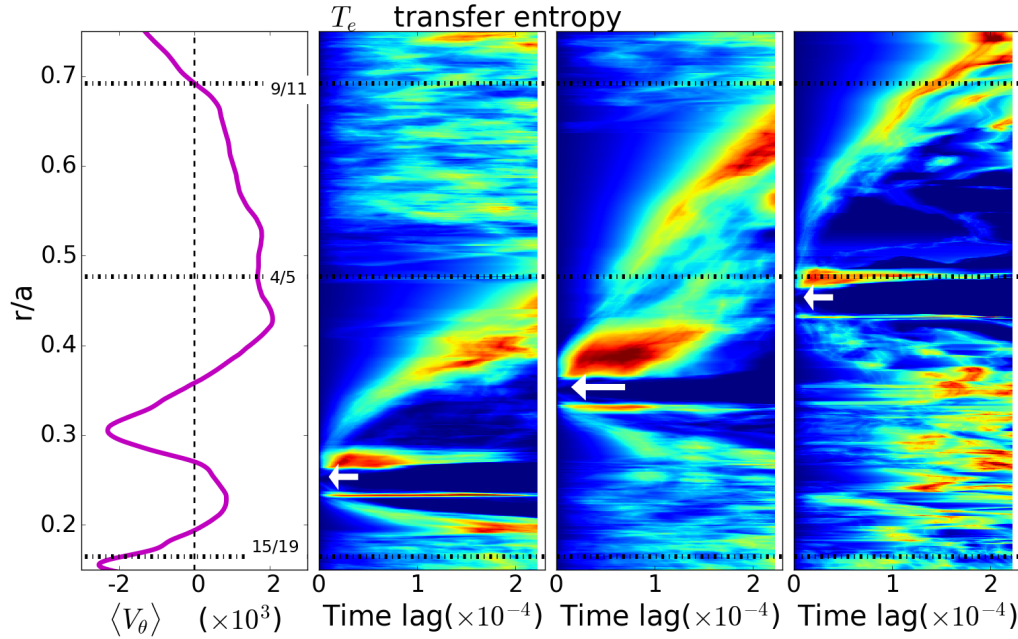
Figure 12. The left panel illustrates the $\langle V_\theta \rangle$. The next three right panels shows the propagation of the perturbation of the electron temperature due to pulses launched at $r/a = 0.25$, $r/a = 0.35$ and $r/a = 0.45$, respectively. Horizontal dashed lines indicate some major rational surfaces.

$r/a \approx 0.4$, due to the shear in the poloidal velocity. The first pulse, launched at $r/a = 0.25$, is mainly trapped by the barrier. However, some part of the pulse crosses the barrier. The pulse slows down around $r/a \approx 0.35$ due to the high flow shear. The second pulse, launched at $r/a = 0.35$, is located initially inside the transport barrier. Part of the pulse remains trapped close to the initial position because of the flow shear, while the rest propagates radially outwards. The last pulse, launched at $r/a = 0.45$. is more clearly outside the transport barrier, so the pulse is not trapped and also propagates mainly outwards. Note that the second and the third pulse also slow down at a different transport barrier that appears to exist around $r/a = 0.55$, where another (small) shear region is present so that propagation slows down.

Next, we use the transfer entropy method to analyze the T_e perturbations. However, the method is quite sensitive to background details, so, to eliminate noise and obtain robust results, we run the same cases eight times and then calculate the average of the transfer entropy results. The eight simulations are run in steady state but at different times with a slightly different background.

Fig. 13 shows the result of the analysis using the Transfer Entropy. As before, the left panel shows the average poloidal velocity. The other three panels show the Transfer Entropy for the three different pulses located at $r/a = 0.25$, $r/a = 0.35$ and $r/a = 0.45$, respectively. The white arrows indicate the position of the reference signal used to compute the Transfer Entropy. This position coincides with the initial radial location

Figure 13. The left panel illustrates the $\langle V_\theta \rangle$. The next three right panels show the Transfer Entropy versus time lag, for the cases corresponding to the pulses launched at $r/a = 0.25$, $r/a = 0.35$ and $r/a = 0.45$, respectively.

of the pulse, facilitating the analysis of the time evolution of the pulse. In the case $r/a = 0.25$, radial propagation from $r/a \approx 0.30$ to $r/a \approx 0.40$ is visible. Furthermore, the horizontal branch of relatively high TE values at $r/a \approx 0.39$ shows that part of the pulse is trapped in that region because of the flow shear. High entropy areas are also present in other regions of the plasma, presumably due to non-local effects. Analysis of the second pulse, launched at $r/a = 0.35$, again show high TE values at $r/a \approx 0.39$, revealing a trapping region, and radial propagation from $r/a \approx 0.45$ to $r/a \approx 0.6$. The TE shows that propagation slows down slightly at $r/a \approx 0.55$ due to the increased flow shear in that region. The last pulse, launched at $r/a = 0.45$, outside the mentioned transport barrier, again shows radial propagation from the initial point to $r/a \approx 0.7$, but there is a region around $r/a \approx 0.68$ where the pulse slows down because of the flow shear associated with a different barrier. In all three cases, the TE shows 'barriers' (horizontal features in the graphs) and 'jumps' (a more intense response at some outward positions than at some positions further inward) during the radial propagation.

5. Discussion

The main results of this work mirror the earlier findings in TJ-II [3]: (a) flow shear layers associated with rational surfaces have an impact on radial heat transport by constituting minor transport barriers, and (b) occasionally transport appears to 'jump over' radial regions, resulting in non-local transport effects. Both these points imply a significant role of magnetic (MHD) turbulence in heat transport in these low density discharges. Consequently, transport is not smooth and continuous, as assumed in most (diffusive) transport models, but heat has a tendency to accumulate at 'trapping zones' located near rational surfaces or perform rapid radial excursions. At least part of the heat transport occurs therefore in a stepwise rather than continuous fashion. The 'jumping' effect is associated with (MHD) mode coupling, involving the exchange of energy between the plasma and the magnetic field [33, 34]. Interestingly, the 'jumps' increase in importance as power is increased.

Spontaneous perturbations and heat waves (due to modulation) both propagate outward at a speed of around 25 m/s. In comparison, outward propagation at TJ-II occurs at a typical speed of 100-200 m/s. This difference can doubtless be associated with the better confinement properties of W7-X. A careful comparison of the analysis of ECRH modulation experiments using both a traditional Fourier technique and the Transfer Entropy clarifies that the time lag of the Transfer Entropy delivers essentially the same information as the Fourier phase delay, justifying our interpretation of the Transfer Entropy in terms of heat transport.

The low-density ECRH heated discharges studied here (Core Electron Root Confinement, CERC) are characterized by a positive radial electric field E_r in the core (electron root) and a negative E_r in the outer half of the plasma (ion root) [10]. The transition between these two regions constitutes a shear layer that might in principle be associated with a transport barrier. The radial position where the Neoclassical radial electric field changes sign (around mid-radius) is expected to shrink by about 30% when power is reduced from its highest to its lowest value [35]. The results shown in Section 3.2, however, show no difference at all in the radial location of the 'trapping zones' as heating power is changed. Hence, it appears unlikely that the Neoclassical change of root is related to the 'trapping zones' reported here. A further argument against a Neoclassical explanation for the observed 'trapping zones' is the simultaneous existence of two radial 'trapping zones' in a single discharge, which cannot easily be explained by the single sign change of E_r predicted by Neoclassical calculations. The main difference between a Neoclassical flow shear layer and one associated with rational surfaces is that the latter is associated with the electromagnetic (fluctuating) component of the fields, which is thought to be essential for the effects reported in this work.

A resistive MHD model has been used to interpret the experimental results. Three different temperature perturbations were launched at different radial locations in the plasma. Radial propagation was always observed. However, the propagation was modified by the shear flows present in the plasma. Analysis of the Transfer Entropy,

applied to these numerical results, showed a clear consistency with the evolution of the electron temperature, confirming the relevance of this technique for the analysis of heat transport. The qualitative success of the model in reproducing the observed phenomenology is ascribed to the fact that it is able to handle perturbations to the magnetic geometry. Nevertheless, this basic model only includes instabilities due to the curvature of the magnetic field and diamagnetic effects. A more realistic description would require a gyro-fluid model more suitable for non-collisional plasmas in toroidal geometry that includes neoclassical damping and various contributions to the heat flux.

This work confirms earlier studies that indicated that rational surfaces have an impact on radial heat transport. A fine study in this respect is the early work carried out at RTP [36]. Also noteworthy is work at Alcator C-Mod [37]. Recently, we performed a study similar to the present one at TJ-II, with similar conclusions [3]. In the future, we plan to study the effect of the mentioned mini-transport barriers on particle transport as well.

Acknowledgements

References

[1] S. Sattler and H.J. Hartfuss. Experimental evidence for electron temperature fluctuations in the core plasma of the W7-AS stellarator. *Phys. Rev. Lett.*, 72:653, 1994. `doi:10.1103/PhysRevLett.72.653`.

[2] A. E. White, L. Schmitz, G. R. McKee, C. Holland, W. A. Peebles, T. A. Carter, M. W. Shafer, M. E. Austin, K. H. Burrell, J. Candy, J. C. DeBoo, E. J. Doyle, M. A. Makowski, R. Prater, T. L. Rhodes, G. M. Staebler, G. R. Tynan, R. E. Waltz, and G. Wang. Measurements of core electron temperature and density fluctuations in DIII-D and comparison to nonlinear gyrokinetic simulations. *Phys. Plasmas*, 15:056116, 2008. `doi:10.1063/1.2895408`.

[3] B.Ph. van Milligen, J.H. Nicolau, L. García, B.A. Carreras, C. Hidalgo, and the TJ-II Team. The impact of rational surfaces on radial heat transport in TJ-II. *Nucl. Fusion*, 57(5):056028, 2017. `doi:10.1088/1741-4326/aa611f`.

[4] P.H. Diamond, S.-I. Itoh, K. Itoh, and T.S. Hahm. Zonal flows in plasma - a review. *Plasma Phys. Control. Fusion*, 47(5):R35, 2005. `doi:10.1088/0741-3335/47/5/R01`.

[5] R. Balescu. *Aspects of anomalous transport in plasmas*. Number Ch. 1.3. Institute of Physics, Bristol, 2005.

[6] P.A. Politzer. Observation of avalanchelike phenomena in a magnetically confined plasma. *Phys. Rev. Lett.*, 84(6):1192, 2000. `doi:10.1103/PhysRevLett.84.1192`.

[7] M. Wanner, J.-H Feist, H. Renner, J. Sapper, F. Schauer, H. Schneider, V. Erckmann, and H. Niedermeyer. Design and construction of Wendelstein 7-X. *Fusion Eng. Des.*, 56–57:155 – 162, 2001. `doi:http://dx.doi.org/10.1016/S0920-3796(01)00239-3`.

[8] R.C. Wolf and The Wendelstein 7-X Team. A stellarator reactor based on the optimization criteria of Wendelstein 7-X. *Fusion Eng. Des.*, 83(7-9):990, 2008. `doi:10.1016/j.fusengdes.2008.05.008`.

[9] R.C. Wolf, A. Ali, A. Alonso, J. Baldzuhn, C. Beidler, M. Beurskens, C. Biedermann, H.-S. Bosch, S. Bozhenkov, R. Brakel, A. Dinklage, Y. Feng, G. Fuchert, J. Geiger, O. Grulke, P. Helander, M. Hirsch, U. Höfel, M. Jakubowski, J. Knauer, G. Kocsis, R. König, P. Kornejew, A. Krämer-Flecken, M. Krychowiak, M. Landreman, A. Langenberg, H.P. Laqua, S. Lazerson, H. Maaßberg, S. Marsen, M. Marushchenko, D. Moseev, H. Niemann, N. Pablant, E. Pasch, K. Rahbarnia, G. Schlisio, T. Stange, T. Sunn Pedersen, J. Svensson, T. Szepesi, H. Trimino Mora, Y. Turkin, T. Wauters, G. Weir, U. Wenzel, T. Windisch, G. Wurden, D. Zhang, I. Abramovic, S. Äkäslompolo, P. Aleynikov, K. Aleynikova, R. Alzbutas, G. Anda, T. Andreeva, E. Ascasibar, J. Assmann, S.-G. Baek, M. Banduch, T. Barbui, M. Barlak, K. Baumann, W. Behr, A. Benndorf, O. Bertuch, W. Biel, D. Birus, B. Blackwell, E. Blanco, M. Blatzheim, T. Bluhm, D. Böckenhoff, P. Bolgert, M. Borchardt, V. Borsuk, J. Boscary, L.-G. Böttger, H. Brand, Ch. Brandt, T. Bräuer, H. Braune, S. Brezinsek, K.-J. Brunner, B. Brünner, R. Burhenn, B. Buttenschön, V. Bykov, I. Calvo, B. Cannas, A. Cappa, A. Carls, L. Carraro, B. Carvalho, F. Castejon, A. Charl, F. Chernyshev, M. Cianciosa, R. Citarella, Ł. Ciupiński, G. Claps, M. Cole, M.J. Cole, F. Cordella, G. Cseh, A. Czarnecka, A. Czermak, K. Czerski, M. Czerwinski, G. Czymek, A. da Molin, A. da Silva, G. Dammertz, J. Danielson, A. de la Pena, S. Degenkolbe, P. Denner, D.P. Dhard, M. Dostal, M. Drevlak, P. Drewelow, Ph. Drews, A. Dudek, G. Dundulis, F. Durodie, P. van Eeten, F. Effenberg, G. Ehrke, M. Endler, D. Ennis, E. Erckmann, H. Esteban, T. Estrada, N. Fahrenkamp, J.-H. Feist, J. Fellinger, H. Fernandes, W.H. Fietz, W. Figacz, J. Fontdecaba, O. Ford, T. Fornal, H. Frerichs, A. Freund, M. Führer, T. Funaba, A. Galkowski, G. Gantenbein, Y. Gao, J. García Regaña, M. Garcia-Munoz, D. Gates, G. Gawlik, B. Geiger, V. Giannella, N. Gierse, A. Gogoleva, B. Goncalves, A. Goriaev, D. Gradic, M. Grahl, J. Green, A. Grosman, H. Grote, M. Gruca, C. Guerard, L. Haiduk, X. Han, F. Harberts, J.H. Harris, H.-J. Hartfuß, D. Hartmann, D. Hathiramani, B. Hein, B. Heinemann, P. Heitzenroeder, S. Henneberg, C. Hennig, J. Hernandez Sanchez, C. Hidalgo, H. Hölbe, K.P. Hollfeld, A. Hölting, D. Höschen, M. Houry, J. Howard, X. Huang,

M. Huber, V. Huber, H. Hunger, K. Ida, T. Ilkei, S. Illy, B. Israeli, A. Ivanov, S. Jablonski, J. Jagielski, J. Jelonnek, H. Jenzsch, P. Junghans, J. Kacmarczyk, T. Kaliatka, J.-P. Kallmeyer, U. Kamionka, R. Karalevicius, H. Kasahara, W. Kasparek, N. Kenmochi, M. Keunecke, A. Khilchenko, D. Kinna, R. Kleiber, T. Klinger, M. Knaup, Th. Kobarg, F. Köchl, Y. Kolesnichenko, A. Könies, M. Köppen, J. Koshurinov, R. Koslowski, F. Köster, R. Koziol, M. Krämer, R. Krampitz, P. Kraszewsk, N. Krawczyk, T. Kremeyer, Th. Krings, J. Krom, G. Krzesinski, I. Ksiazek, M. Kubkowska, G. Kühner, T. Kurki-Suonio, S. Kwak, R. Lang, S. Langish, H. Laqua, R. Laube, C. Lechte, M. Lennartz, W. Leonhardt, L. Lewerentz, Y. Liang, Ch. Linsmeier, S. Liu, J.-F. Lobsien, D. Loesser, J. Loizu Cisquella, J. Lore, A. Lorenz, M. Losert, L. Lubyako, A. Lücke, A. Lumsdaine, V. Lutsenko, J. Majano-Brown, O. Marchuk, M. Mardenfeld, P. Marek, S. Massidda, S. Masuzaki, D. Maurer, K. McCarthy, P. McNeely, A. Meier, D. Mellein, B. Mendelevitch, Ph. Mertens, D. Mikkelsen, O. Mishchenko, B. Missal, J. Mittelstaedt, T. Mizuuchi, A. Mollen, V. Moncada, T. Mönnich, T. Morizaki, R. Munk, S. Murakami, F. Musielok, G. Náfrádi, M. Nagel, D. Naujoks, H. Neilson, O. Neubauer, U. Neuner, T. Ngo, R. Nocentini, C. Nührenberg, J. Nührenberg, S. Obermayer, G. Offermanns, K. Ogawa, J. Ongena, J.W. Oosterbeek, G. Orozco, M. Otte, L. Pacios Rodriguez, W. Pan, N. Panadero, N. Panadero Alvarez, A. Panin, D. Papenfuß, S. Paqay, A. Pavone, E. Pawelec, G. Pelka, X. Peng, V. Perseo, B. Peterson, A. Pieper, D. Pilopp, S. Pingel, F. Pisano, B. Plaum, G. Plunk, M. Povilaitis, J. Preinhaelter, J. Proll, M.-E. Puiatti, A. Puig Sitjes, F. Purps, M. Rack, S. Récsei, A. Reiman, D. Reiter, F. Remppel, S. Renard, R. Riedl, J. Riemann, S. Rimkevicius, K. Riße, A. Rodatos, H. Röhlinger, M. Romé, P. Rong, H.-J. Roscher, B. Roth, L. Rudischhauser, K. Rummel, T. Rummel, A. Runov, N. Rust, L. Ryc, S. Ryosuke, R. Sakamoto, A. Samartsev, M. Sanchez, F. Sano, S. Satake, G. Satheeswaran, J. Schacht, F. Schauer, T. Scherer, A. Schlaich, K.-H. Schlüter, J. Schmitt, H. Schmitz, O. Schmitz, S. Schmuck, M. Schneider, W. Schneider, M. Scholz, P. Scholz, R. Schrittwieser, M. Schröder, T. Schröder, R. Schroeder, H. Schumacher, B. Schweer, B. Shanahan, I.V. Shikhovtsev, M. Sibilia, P. Sinha, S. Sipliä, J. Skodzik, C. Slaby, H. Smith, W. Spiess, D.A. Spong, A. Spring, R. Stadler, B. Standley, L. Stephey, M. Stoneking, U. Stridde, Z. Sulek, C. Surko, Y. Suzuki, V. Szabó, T. Szabolics, Z. Szökefalvi-Nagy, N. Tamura, A. Terra, J. Terry, J. Thomas, H. Thomsen, M. Thumm, C.P. von Thun, D. Timmermann, P. Titus, K. Toi, J.M. Travere, P. Traverso, J. Tretter, H. Tsuchiya, T. Tsujimura, S. Tulipán, M. Turnyanskiy, B. Unterberg, J. Urban, E. Urbonavicius, I. Vakulchyk, S. Valet, B. van Millingen, L. Vela, J.-L. Velasco, M. Vergote, M. Vervier, N. Vianello, H. Viebke, R. Vilbrandt, A. Vorkörper, S. Wadle, F. Wagner, E. Wang, N. Wang, F. Warmer, L. Wegener, J. Weggen, Y. Wei, J. Wendorf, A. Werner, B. Wiegel, F. Wilde, E. Winkler, V. Winters, S. Wolf, J. Wolowski, A. Wright, P. Xanthopoulos, H. Yamada, I. Yamada, R. Yasuhara, M. Yokoyama, J. Zajac, M. Zarnstorff, A. Zeitler, H. Zhang, J. Zhu, M. Zilker, A. Zimbal, A. Zocco, S. Zoletnik, and M. Zuin. Major results from the first plasma campaign of the Wendelstein 7-X stellarator. *Nuclear Fusion*, 57(10):102020, 2017. `doi:10.1088/1741-4326/aa770d`.

[10] A. Dinklage, A. Alonso, J. Baldzuhn, C.D. Beidler, C. Biedermann, B. Blackwell, S. Bozhenkov, R. Brakel, B. Buttenschön, Y. Feng, G. Fuchert, J. Geiger, P. Helander, M. Hirsch, U. Hoefel, J. Knauer, A. Krämer-Flecken, M. Landreman, A. Langenberg, H.P. Laqua, H. Maaßberg, N.A. Pablant, E. Pasch, K. Rahbarnia, L. Rudischhauser, H. Smith, T. Stange, L. Stephey, H. Trimino-Mora, Yu. Turkin, J.-L. Velasco, G. Wurden, D. Zhang, T. Andreeva, M. Beurskens, E. Blanco, H.-S. Bosch, R. Burhenn, A. Cappa, A. Czarnecka, M. Dostal, P. Drews, M. Endler, T. Estrada, T. Fornal, O. Grulke, D. Hartmann, J.H. Harris, M. Jakubowski, T. Klinger, S. Klose, G. Kocsis, R. König, P. Kornejew, N. Krawczyk, M. Krychowiak, M. Kubkowska, I. Ksiazek, S. Lazerson, Y. Liang, S. Liu, O. Marchuk, S. Marsen, N. Marushchenko, V. Moncada, D. Moseev, D. Naujoks, H. Niemann, M. Otte, T.S. Pedersen, F. Pisano, K. Riße, T. Rummel, O. Schmitz, S. Satake, T. Schröder, T. Szepesi, H. Thomsen, P. Traverso, H. Tsuchiya, P. Valson, N. Wang, T. Wauters, G. Weir, R. Wolf, M. Yokoyama, and the W7-X Team. Core

confinement in Wendelstein 7-X limiter plasmas. In *ECA*, volume 40A, page O2.107, 2016. URL: `http://ocs.ciemat.es/EPS2016PAP/pdf/O2.107.pdf`.

[11] Thomas Sunn Pedersen, Andreas Dinklage, Yuriy Turkin, Robert Wolf, Sergey Bozhenkov, Joachim Geiger, Golo Fuchert, Hans-Stephan Bosch, Kian Rahbarnia, Henning Thomsen, Ulrich Neuner, Thomas Klinger, Andreas Langenberg, Humberto Trimiño Mora, Petra Kornejew, Jens Knauer, Matthias Hirsch, the W-X Team, and Novimir Pablant. Key results from the first plasma operation phase and outlook for future performance in Wendelstein 7-X. *Phys. Plasmas*, 24(5):055503, 2017. `doi:10.1063/1.4983629`.

[12] A. Dinklage. Private communication.

[13] T. Klinger, A. Alonso, S. Bozhenkov, R. Burhenn, A. Dinklage, G. Fuchert, J. Geiger, O. Grulke, A. Langenberg, M. Hirsch, G. Kocsis, J. Knauer, A. Krämer-Flecken, H. Laqua, S. Lazerson, M. Landreman, H. Maaßberg, S. Marsen, M. Otte, N. Pablant, E. Pasch, K. Rahbarnia, T. Stange, T. Szepesi, H. Thomsen, P. Traverso, J. L Velasco, T. Wauters, G. Weir, T. Windisch, and The Wendelstein 7-X Team. Performance and properties of the first plasmas of Wendelstein 7-X. *Plasma Phys. Control. Fusion*, 59:014018, 2017. `doi:10.1088/0741-3335/59/1/014018`.

[14] N.B. Marushchenko, A. Dinklage, H.J. Hartfuss, M. Hirsch, H. Maassberg, and Yu. Turkin. Optimization of ECE diagnostics for the W7-X stellarator. *Fusion Sci. Technol.*, 50(3):395, 2006. URL: `http://epubs.ans.org/?a=1261`.

[15] R. König, J. Baldzuhn, W. Biel, C. Biedermann, H.S. Bosch, S. Bozhenkov, T. Bräuer, B. Brotas de Carvalho, R. Burhenn, B. Buttenschön, G. Cseh, A. Czarnecka, M. Endler, V. Erckmann, T. Estrada, J. Geiger, O. Grulke, D. Hartmann, D. Hathiramani, M. Hirsch, S. Jabłonski, M. Jakubowski, J. Kaczmarczyk, T. Klinger, S. Klose, G. Kocsis, P. Kornejew, A. Krämer-Flecken, T. Kremeyer, M. Krychowiak, M. Kubkowska, A. Langenberg, H. P. Laqua, M. Laux, Y. Liang, A. Lorenz, A.O. Marchuk, V. Moncada, O. Neubauer, U. Neuner, J.W. Oosterbeek, M. Otte, N. Pablant, E. Pasch, T.S. Pedersen, K. Rahbarnia, L. Ryc, O. Schmitz, W. Schneider, H. Schuhmacher, B. Schweer, T. Stange, H. Thomsen, J.-M. Travere, T. Szepesi, U. Wenzel, A. Werner, B. Wiegel, T. Windisch, R. Wolf, G.A. Wurden, D. Zhang, A. Zimbal, S. Zoletnik, and the W7-X Team. The set of diagnostics for the first operation campaign of the Wendelstein 7-X stellarator. *Journal of Instrumentation*, 10(10):P10002, 2015. `doi:10.1088/1748-0221/10/10/P10002`.

[16] G. Kocsis, A. Alonso, C. Biedermann, G. Cseh, A. Dinklage, M. Jakubowski, R. König, M. Krychowiak, M. Otte, T. Sunn Pedersen, T. Szepesi, S. Zoletnik, and the W7-X Team. Investigation of edge filament dynamics in W7-X limiter plasmas. In *ECA*, volume 40A, page P4.003, 2016. URL: `http://ocs.ciemat.es/EPS2016PAP/pdf/P4.003.pdf`.

[17] B.Ph. van Milligen, A. Lopez Fraguas, M.A. Pedrosa, C. Hidalgo, A. Martín de Aguilera, and E. Ascasíbar. Parallel and perpendicular turbulence correlation length in the TJ-II stellarator. *Nucl. Fusion*, 53:093025, 2013. `doi:10.1088/0029-5515/53/9/093025`.

[18] L. García, M.A. Ochando, B. A. Carreras, D. Carralero, C. Hidalgo, and B. Ph. van Milligen. Effect of fast electrons on the stability of resistive interchange modes in the TJ-II stellarator. *Phys. Plasmas*, 23:062319, 2016. `doi:10.1063/1.4954826`.

[19] I. Teliban, D. Block, A. Piel, and F. Greiner. Improved conditional averaging technique for plasma fluctuation diagnostics. *Plasma Phys. Control. Fusion*, 49:485, 2007. `doi:10.1088/0741-3335/49/4/011`.

[20] T. Schreiber. Measuring information transfer. *Phys. Rev. Lett.*, 85(2):461, 2000. `doi:10.1103/PhysRevLett.85.461`.

[21] B.Ph. van Milligen, G. Birkenmeier, M. Ramisch, T. Estrada, C. Hidalgo, and A. Alonso. Causality detection and turbulence in fusion plasmas. *Nucl. Fusion*, 54:023011, 2014. `doi:10.1088/0029-5515/54/2/023011`.

[22] B.Ph. van Milligen, B.A. Carreras, L. García, A. Martin de Aguilera, C. Hidalgo, J.H. Nicolau, and the TJ-II Team. The causal relation between turbulent particle flux and density gradient. *Phys. Plasmas*, 23:072307, 2016. `doi:10.1063/1.4958806`.

[23] U. Höfel, S. Bozhenkov, G. Fuchert, J. Geiger, H.-J. Hartfuss, M. Hirsch, F. Köster, H. Maassberg, N. B. Marushchenko, E. Pasch, S. Schmuck, T. Stange, H. Tsuchiya, Y. Turkin, J.-L. Velasco, G. M. Weir, R. Wolf, and the W7-X Team. First measurement on electron heat transport by heatwaves in the core plasma of Wendelstein 7-X. In *ECA*, volume 40A, page P4.008, 2016. URL: `http://ocs.ciemat.es/EPS2016PAP/pdf/P4.008.pdf`.

[24] A. Jacchia, P. Mantica, F. De Luca, and G. Gorini. Determination of diffusive and nondiffusive transport in modulation experiments in plasmas. *Phys. Fluids B*, 3:3033, 1991. `doi:10.1063/1.859781`.

[25] A. Thyagaraja. Numerical simulations of tokamak plasma turbulence and internal transport barriers. *Plasma Phys. Control. Fusion*, 42:B255, 2000. `doi:10.1088/0741-3335/42/12B/320`.

[26] R.C. Wolf. Internal transport barriers in tokamak plasmas. *Plasma Phys. Control. Fusion*, 45:R1, 2003. `doi:10.1088/0741-3335/45/1/201`.

[27] J.W. Connor, T. Fukuda, X. Garbet, C. Gormezano, V. Mukhovatov, M. Wakatani, and the ITB Database Group and the ITPA Topical Group on Transport and Internal Barrier Physics. A review of internal transport barrier physics for steady-state operation of tokamaks. *Nucl. Fusion*, 44:R1, 2004. `doi:10.1088/0029-5515/44/4/R01`.

[28] B.A. Carreras, I. Llerena Rodríguez, and L. García. Topological structures of the resistive pressure gradient turbulence with averaged poloidal flow. *Nucl. Fusion*, 54:103005, 2014. `doi:10.1088/0029-5515/54/10/103005`.

[29] A.M. Garofalo, X. Gong, B.A. Grierson, Q. Ren, W.M. Solomon, E.J. Strait, M.A. Van Zeeland, C.T. Holcomb, O. Meneghini, S.P. Smith, G.M. Staebler, B. Wan, R. Bravenec, R.V. Budny, S. Ding, J.M. Hanson, W.W. Heidbrink, L.L. Lao, G. Li, C. Pan, C.C. Petty, J. Qian, C. Paz-Soldan, and G. Xu. Compatibility of internal transport barrier with steady-state operation in the high bootstrap fraction regime on DIII-D. *Nucl. Fusion*, 55(12):123025, 2015. `doi:10.1088/0029-5515/55/12/123025`.

[30] L. García, I. Llerena Rodríguez, and B.A. Carreras. Width and rugosity of the topological plasma flow structures and their relation to the radial flights of particle tracers. *Nucl. Fusion*, 55(11):113023, 2015. `doi:10.1088/0029-5515/55/11/113023`.

[31] L. García, B.A. Carreras, V.E. Lynch, M.A. Pedrosa, and C. Hidalgo. Sheared flow amplification by vacuum magnetic islands in stellarator plasmas. *Phys. Plasmas*, 8(9):4111, 2001. `doi:10.1063/1.1392996`.

[32] H.R. Strauss. Nonlinear, threedimensional magnetohydrodynamics of noncircular tokamaks. *Phys. Fluids*, 19:134, 1976. `doi:10.1063/1.861310`.

[33] J.D. Callen and M.W. Kissick. Evidence and concepts for non-local transport. *Plasma Phys. Control. Fusion*, 39:B173, 1997. `doi:10.1088/0741-3335/39/12B/014`.

[34] V.D. Pustovitov. Nonlocal effects in energy balance in an equilibrium plasma during its fast heating/cooling in tokamaks and stellarators. *Plasma Phys. Control. Fusion*, 54(12):124036, 2012. `doi:10.1088/0741-3335/54/12/124036`.

[35] N.A. Pablant, A. Dinklage, M. Landreman, A. Langenberg, A. Alonso, C.D. Beidler, M. Beurskens, M. Bitter, S. Bozhenkov, R. Burhenn, L.F. Delgado-Aparicio, G. Fuchert, D.A. Gates, J. Geiger, K.W. Hill, U. Hoefel, M. Hirsch, J. Knauer, A. Krämer-Flecken, S. Lazerson, H. Maassberg, O. Marchuk, N.B. Marushchenko, D.R. Mikkelsen, E. Pasch, S. Satake, H. Smith, J. Svensson, P. Traverso, Y. Turkin, P. Valson, J.L. Velasco, G. Weir, T. Windisch, R.C. Wolf, M. Yokoyama, D. Zhang, and the W7-X Team. Investigation of the core radial electric field in Wendelstein 7-X plasmas. In *ECA*, volume 40A, page P4.013, 2016. URL: `http://ocs.ciemat.es/EPS2016PAP/pdf/P4.013.pdf`.

[36] N.J. Lopes Cardozo, G.M.D. Hogeweij, M. de Baar, C.J. Barth, M.N.A. Beurskens, F. De Luca, A.J.H. Donné, P. Galli, J.F.M. van Gelder, G. Gorini, B. de Groot, A. Jacchia, F.A. Karelse, J. de Kloe, O.G. Kruijt, J. Lok, P. Mantica, H.J. van der Meiden, A.A.M. Oomens, Th. Oyevaar, F.J. Pijper, R.W. Polman, F. Salzedas, F.C. Schüller, and E. Westerhof. Electron thermal transport in RTP: filaments, barriers and bifurcations. *Plasma Phys. Control. Fusion*, 39:B303,

1997. `doi:10.1088/0741-3335/39/12B/023`.

[37] S.J. Wukitch, R.L. Boivin, P.T. Bonoli, C.L. Fiore, R.S. Granetz, M.J. Greenwald, A.E. Hubbard, I.H. Hutchinson, Y. In, J. Irby, Y. Lin, E.S. Marmar, D. Mossessian, M. Porkolab, G. Schilling, J.E. Rice, J.A. Snipes, S.M. Wolfe, and Alcator C-Mod group. Double transport barrier experiments on Alcator C-Mod. *Phys. Plasmas*, 9:2149, 2002. `doi:10.1063/1.1467347`.